High-Speed Avalanche Photodiodes With Wide Dynamic Range Performance

Hao-Yi Zhao, Naseem, Andrew H. Jones, Rui-Lin Chao, Zohauddin Ahmad, Joe C. Campbell, *Fellow, IEEE*, and Jin-Wei Shi, *Senior Member, IEEE*

***Abstract*—In this work, we demonstrate a novel top-illuminated avalanche photodiode (APD) with high-speed and wide dynamic range performance for coherent lidar applications, which needs simultaneous processing of weak light reflections from the object and a strong optical local-oscillator (LO) signal at the receiving end. By taking advantage of a partially depleted p-type $In_{0.53}Ga_{0.47}As$ absorbing layer and a thin $In_{0.52}Al_{0.48}As$ multiplication layer (88 nm), the demonstrated APDs exhibit a wide optical-to-electrical bandwidth (16 GHz) and high responsivity (2.5 A/W at 0.9 V_{br}) near the saturation output current which is as high as >8 mA. Furthermore, the measured low excess noise (k = 0.14) characteristics of this device ensure its wide dynamic range performance. In addition, it should be noted that the measured nonlinear behaviors of these APDs are quite different from those of typical fast p-i-n photodiodes (PDs), which always show serious degradation in their O-E bandwidths at their saturation output. On the other hand, the measured bias dependent 3-dB O-E bandwidth of the demonstrated APDs can be pinned at 16 GHz without any degradation at around the saturation current output. Such distinct nonlinear APD behaviors can be attributed to the space-charge-screening effect induced gain reduction under high-power operation.**

***Index Terms*—Avalanche photodiode, photodiode.**

I. Introduction

THE development of lidar has been booming recently especially for use in autonomous cars, robots, and unmanned aerial vehicles, anywhere it is necessary to monitor both fast moving and fixed objects in real time. 3-dimensional (3-D) lidar plays a critical sensing role to attain this goal [1]. To date, most of the commercially available lidar systems incorporate the direct detection (DD) time-of-flight (ToF) sensors operating at 905 nm [1], [2]. However, these sensors suffer from two major problems. One is eye-safety, which limits maximum laser powers and hence operating range, and the other is potential interference issues when the lidar systems of lots of cars are operating simultaneously. By shifting the operating wavelength from 905 nm to the telecommunication window (∼1.51 μm), the afore-mentioned eye-safety issue can be remedied [3]–[6]. Furthermore, by introducing the well-developed coherent detection scheme in the telecommunication window (1.31 to 1.55 μm), coherent lidar systems with improved signal-to-noise (S/N) ratios and stronger immunity to interference have been successfully demonstrated [3]–[6].

In contrast to a DD lidar system, which requires avalanche photodiodes (APDs) operated in Geiger mode for single-photon detection [7], a heterodyne or homodyne frequency-modulated continuous-wave (FMCW) coherent lidar system usually needs p-i-n photodiodes (PDs) with a wide optical-to-electrical (O-E) bandwidth, high responsivity and high saturation power [4]–[6]. In these systems, strong optical pumping power (>10 mW) from the local-oscillator (LO) source is usually preferred to enhance the S/N ratio of the down-converted intermediate frequency (IF) signal from p-i-n PD, which has high saturation output. High-power waveguide type uni-traveling carrier photodiodes (UTC-PDs), which are monolithically integrated with the semiconductor optical amplifier (SOA) have been developed and successfully demonstrated [8], [9] for application in a coherent communication system. However, for the coherent lidar receivers, the optical aperture size of the waveguide type PD is usually too small to capture the weak light reflected from the object; the vertical-illuminated type PD is more suitable for such applications. The sensitivity performance of the APDs in a DD system can be around 8 dB higher (at 10 Gbit/sec operation) than that of the p-i-n PDs. However, the saturation current of the APD is usually much smaller than that of the p-i-n PD under strong light pumping due to the process of additional carrier multiplication in the APD's active layer. This impedes its application in coherent receivers. Nevertheless, in modern chip scale [10] or photonic integrated circuit (PIC) lidars [5], [11], the on-chip optical LO power is usually very limited and most of the LO power must be allocated to the transmitting side to compensate for the significant propagation and scattering loss in free space for long range (hundreds of meter) sensing. APDs, which have a wide-dynamic range and higher responsivity than that of p-i-n PDs under a medium optical LO pumping power (∼1 mW) are thus highly desired for this kind of application. In addition, the wide O-E bandwidth in these APDs may also be preferred due that to in the advanced distributed feedback

Manuscript received July 15, 2019; revised September 7, 2019; accepted September 24, 2019. Date of publication September 26, 2019; date of current version November 27, 2019. This work was supported in part by the Ministry of Science and Technology in Taiwan under Grants 108-2622-E-008 -011 -CC2, 107-2622-E-008 -002 -CC2, and 106-2221-E-008 -063 -MY3. *(Corresponding author: Jin-Wei Shi.)*

H.-Y. Zhao, Naseem, Z. Ahmad, and J.-W. Shi are with the Department of Electrical Engineering, National Central University, Taoyuan 320, Taiwan (e-mail: wl01775306as@yahoo.com.tw; naseemever3@gmail.com; zohauddin145991@st.jmi.ac.in; jwshi@ee.ncu.edu.tw).

A. H. Jones and J. C. Campbell are with the Department of Electrical and Computer Engineering, University of Virginia, Charlottesville, VA 22904 USA (e-mail: ahj2ge@virginia.edu; jcc7s@virginia.edu).

R.-L. Chao is with the Department of Photonics, National Chiao-Tung University, Hsinchu 300, Taiwan (e-mail: obscurotation.eo03g@g2.nctu.edu.tw).

Color versions of one or more of the figures in this article are available online at http://ieeexplore.ieee.org.

Digital Object Identifier 10.1109/JLT.2019.2944098

(DFB) or distributed Bragg reflector (DBR) lasers, the wavelength ramping (sweeping) rate (γ) can be as high as tens to hundreds of GHz per μs [10], [12]. For the case of ns to μs optical round-trip time (τ_{R}) delay time in FMCW lidar driven by the afore-mentioned light source, the corresponding homodyne beating frequency ($\gamma\tau_{\mathrm{R}}$) might range from between several GHz to tens of GHz [13].

In this work, we demonstrate a novel vertical-illuminated APD. The demonstrated APDs fabricated using a partially depleted p-type $In_{0.53}Ga_{0.47}As$ absorbing layer and thin $In_{0.52}Al_{0.48}As$ multiplication layer (88 nm) exhibit a wide optical-to-electrical bandwidth (18 GHz at $0.9V_{\mathrm{br}}$), large gain-bandwidth product (459 GHz), low excess noise (k = 0.14), and a saturation current as high as 8 mA. These dynamic performances are superior to those of the APDs reported in our previous work [14] due to the downscaling of absorption layer thickness. The measured bias dependent 3-dB O-E bandwidth of the newly demonstrated APDs can be pinned at 16 GHz with a 2.5 A/W responsivity at around the saturation current output and 0.9 V_{br}, which differs quite a bit from the nonlinear behaviors of the p-i-n PDs. Saturation in the DC output photocurrent of the p-i-n PD is usually accompanied by serious degradation in its O-E bandwidth. The excellent dynamic characteristics of the demonstrated APDs give them the potential to replace p-i-n PDs in chip-scale and PIC coherent FMCW lidar receivers [10], [11].

II. Design of Device Structure and Fabrication

Here, the static and dynamic behaviors of two kinds of devices (A and B) are studied in detail. Fig. 1(a) and (b) show conceptual cross-sectional views of demonstrated devices A and B, respectively, with their top-illuminated structure. Both devices have the same design of epi-layer structure but different absorption layer thicknesses in order to compare their high-power performance. Note that this figure is not drawn in scale. From top to bottom, the structure of both device is composed of the p^+-$In_{0.53}Ga_{0.47}As$ contact layer, p^+-InP window layer, p-type partially depleted $In_{0.53}Ga_{0.47}As$ absorbing layer, two p-type $In_{0.52}Al_{0.48}As$ charge layers, one intrinsic $In_{0.52}Al_{0.48}As$ field buffer layer, one intrinsic $In_{0.52}Al_{0.48}As$ M- layer, and N^+ $In_{0.52}Al_{0.48}As$ /InP contact layers. Here, the partially depleted p-type absorber, which has a graded doping profile in the p-type layer (top: 1×10^{19} to bottom: $1 \times 10^{17}\mathrm{cm}^{-3}$) is used to shorten the hole transit time, accelerate the electron diffusion process, and increase the high-power and linearity performance of our APD [15]. In order to shorten the avalanche delay time, the M-layer is thin, around 90 nm, in both device structures [15]. The minimum M-layer thickness in our APDs is limited by the significant Zener breakdown and huge dark current, which would vanish the avalanche gain and the high-sensitivity performance of the APDs. For more detail about the epi-layer structure and the working principles of the demonstrated APDs, the interested reader can refer to our previous works [16], [17]. Here, the total thicknesses of the $In_{0.53}Ga_{0.47}As$ absorption layers for devices A and B are 0.4 and 0.8 μm, respectively. One of the most effective way to minimize the space-charge-screening (SCS) effect inside the active layers and enhance the saturation

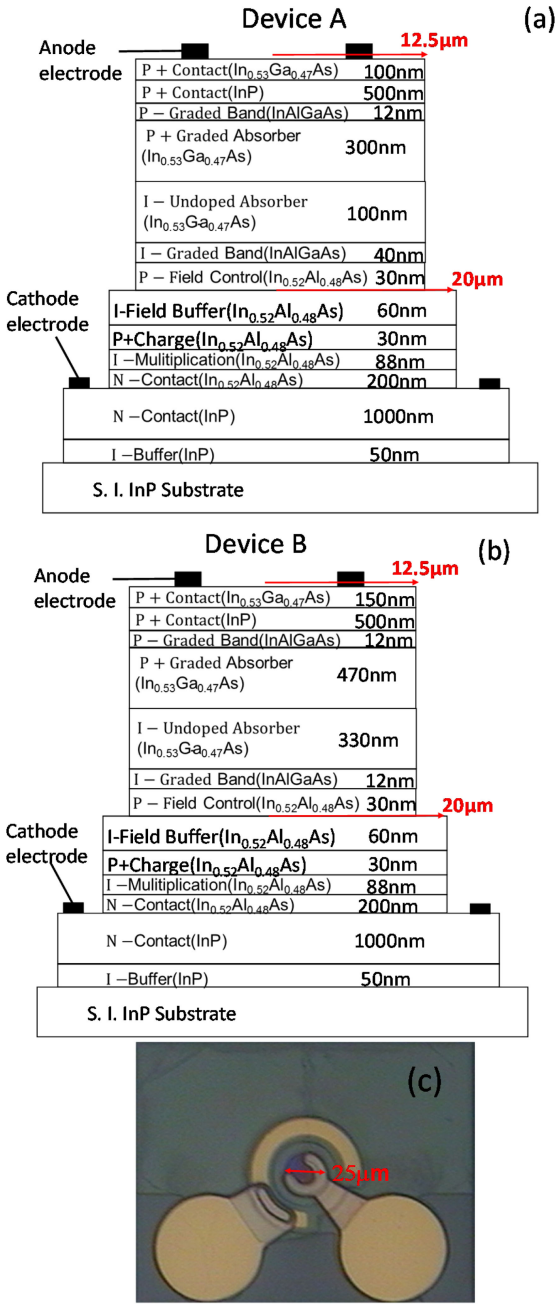

Fig. 1. Conceptual cross-sectional view of the demonstrated (a) device A and (b) device B. The radius of the active mesa is 12.5 μm, as specified in this figure. (c) Top-view of the fabricated devices.

output current is to thin down the thickness of the depleted photo-absorption layer in the fast p-i-n photodiode [18], [19]. Here, we want to investigate the influence of the depletion layer thickness on the high-power performance of our demonstrated APDs.

As shown in Fig. 1, the same triple mesa structure is adopted for both devices A and B. The first mesa with a diameter of 25 μm is etched through the upper charge (field-control) layer and stops at the 60 nm $In_{0.52}Al_{0.48}As$ buffer layer. The additional charge layer in the upper mesa is expected to effectively confine the strong electric (E)-field in the bottom M-layer within the

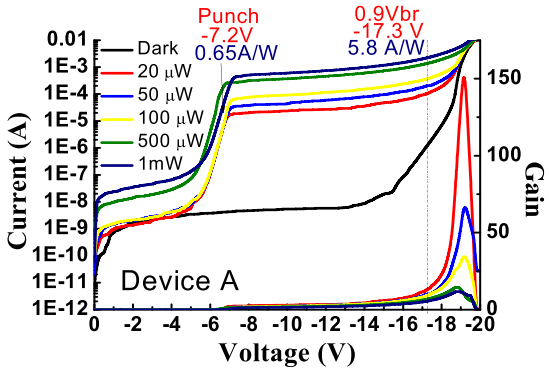

Fig. 2. The measured dark current, photocurrent, and operation gain versus bias voltages under different optical pumping powers of device A at the 1.31 μm wavelength.

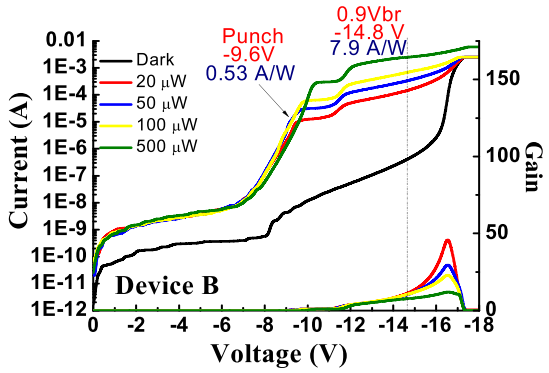

Fig. 3. The measured dark current, photocurrent, and operation gain versus bias voltages under different optical pumping powers of device B at the 1.31 μm wavelength.

range of the 25 μm diameter. For detailed E-field distributions for our device structure please refer to our previous work [16]. Fig. 1(c) shows the top-view of the device fabricated with a 25 μm diameter active mesa. The diameter of the active optical window is 12 μm.

III. Measurement Results

Figs. 2 and 3 show the measured bias-dependent dark current, photocurrent, and operation gain of devices A and B, respectively, subjected to different optical pumping powers at an optical wavelength of 1.31 μm. As can be seen, although both devices have the same M-layer design and doping density in the charge layers, there is some difference in their measured breakdown voltage (V_{br}), found to be around -19.5 and -16.5 V for device A and B, respectively. The smaller punch through voltage (V_{pt}) and larger V_{br} of device A suggest a shift in its charge layer doping density toward lower values than for device B. Such a discrepancy in doping density for different runs of APD wafer growth may be minimized by further improving the growth conditions. As can be seen, under 0.9 V_{br} operation, Device B has a higher responsivity than that of device A, because of its thicker absorption layer (0.8 vs. 0.4 μm). However, under V_{pt} operation, the responsivity of device A is even higher than that of

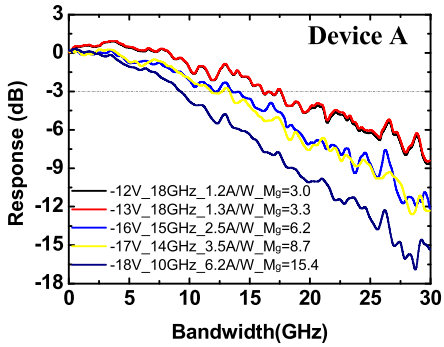

Fig. 4. The measured bias dependent O-E frequency responses of device A under a 50 μW optical pumping power at the 1.31 μm wavelength.

device B. This might be attributable to the thicker $In_{0.53}Ga_{0.47}As$ absorber layer in device B which results in a lower E-field inside its absorption region than is the case for device A when the bias voltage just reaches V_{pt}. This thus leads to the smaller photocurrent and poorer responsivity of device B. Nevertheless, when the reverse bias voltage is further increased, the carrier (electron/hole) drift-velocity becomes saturated so that the measured responsivity is determined by the absorption efficiency and multiplication gain rather than the carrier drift-velocity.

We assume a zero coupling loss and single-pass of injected light into the absorption layer of our device. With a 0.4 (0.8) μm-thick $In_{0.53}Ga_{0.47}As$ absorption layer, the theoretical maximum unit gain responsivity is around 0.4 (0.65) A/W at the 1.31 μm wavelength. Here, the photo-absorption constant used for the $In_{0.53}Ga_{0.47}As$ layer at such a wavelength is around 1.2 μm^{-1} [20]. The gain versus bias voltages of devices A and B under different optical pumping powers (20, 50, 100, 500, and 1000$-\mu$W) are also provided in the figures for reference. As can be seen, there is a significant reduction in all the measured operation gains when the reverse bias voltage is over V_{br} due to the tremendous increase of dark current, which occupies most of the measured total current (i.e., summation of photocurrent and dark current). In addition, we can clearly see that the maximum operation gain gradually decreases with increasing pumping power. This phenomenon can be explained by the space charge screening (SCS) effect induced by the photo-generated holes in the undoped $In_{0.53}Ga_{0.47}As$ absorption layer, which reduce the net E-field and multiplication gain in the M-layer [21]. In addition, the much higher operation gain attained by device A under the same value of optical pumping power compared to device B, can be attributed to the minimization of the SCS by the thinning of the depleted absorption layer thickness [18], [19]. The influence of the SCS effect on the dynamic performance of our demonstrated APDs under high-power operation will be discussed in detail later.

Figs. 4 and 5 show the bias-dependent O-E frequency responses of devices A and B, respectively, measured under a low optical pumping power at the 1.31 μm wavelength (50 and 20$-\mu$W for device A and B, respectively). Under such low optical pumping power, we can clearly see a gradual decrease in the measured O-E bandwidths with an increase of the reverse bias

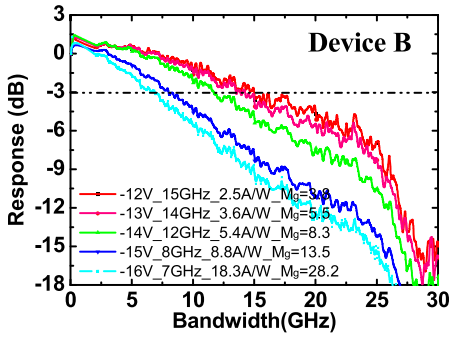

Fig. 5. The measured bias dependent O-E frequency responses of device B under a 20 μW optical pumping power at the 1.31 μm wavelength.

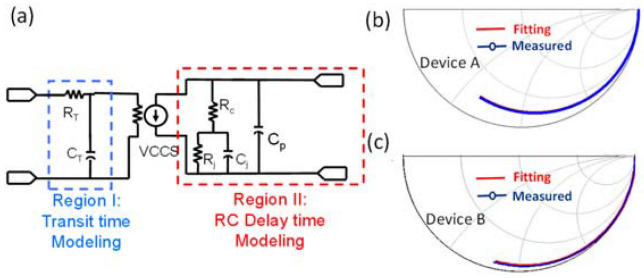

Fig. 6. (a) Equivalent-circuit-model. VCCS: voltage controlled current source. Measured (blue line) and fitted (red line) S_{22} parameters from near dc to 30 GHz under a fixed dc bias (−13 V) for (b) device A and (c) device B.

voltage (operation gain). The maximum 3-dB O-E bandwidths of devices A and B are around 18 and 15 GHz, respectively. The degradation in the O-E bandwidth with the increase of operation gain is very common in APDs, and can be attributed to the increase of the avalanche induced delay time with the gain. Two effective ways to minimize the delay time and enhance the gain-bandwidth product of the APD are thinning down the thickness of the multiplication layer (<100 nm) and choose a material with a large electron/hole ionization coefficient ratio for the multiplication layer [22].

The overall O-E 3-dB bandwidth of an APD under low gain operation is determined by the carrier transport time and the RC time constant. The equivalent circuit modeling technique was used to investigate the dominant bandwidth limiting factor in these two devices [23], [24]. Here, the RC-limited bandwidth can be extracted by using the measured scattering parameters for the microwave reflection coefficients (S_{22}) [23], [24]. Fig. 6(a) shows the equivalent circuit models adopted for fitting of the S_{22} parameters of devices A and B. The fitted values for each circuit element in devices A and B are shown in Table I. During the device modeling process for the extraction of extrinsic f_{RC} of PD chips, the two artificial circuit elements; R_T and C_T, are removed. This is because they are used to mimic the low-pass frequency response of the internal carrier transient time [23], [24]. The fitted and measured frequency responses for the S_{22} parameters for Devices A and B are shown on a Smith chart in Figs. 6(b) and (c), respectively. Clearly, there is a good match

TABLE I
VALUES OF THE CIRCUIT ELEMENTS

	Physical Meaning	A	B
C_j	Junction Capacitance (fF)	155	80
R_j	Junction Resistance (kΩ)	>600	>600
R_C	Contact Resistance (Ω)	8	6
C_P	Parasitic Capacitance (fF)	15	52

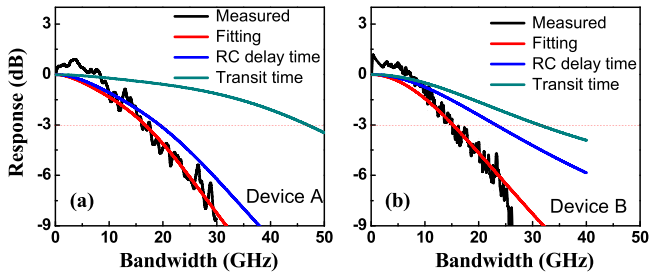

Fig. 7. The measured O-E, extracted RC-limited, transient time, and fitted O-E frequency responses of devices (a) A and (b) B.

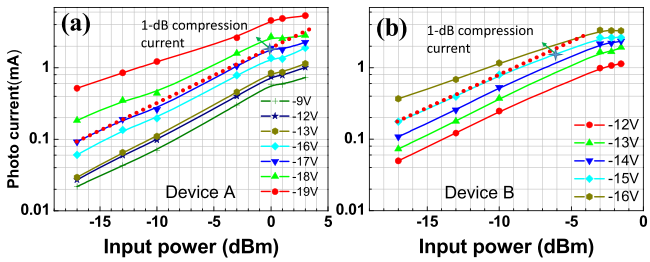

Fig. 8. The measured DC output photocurrent versus input optical power of (a) device A and (b) device B at the 1.31 μm wavelength.

between the simulated and measured results from 40 MHz to 30 GHz.

By use of the extracted equivalent circuit model and choosing the proper values of R_T and C_T to fit the measured O-E frequency response, we can then determine the internal transient time limited frequency responses of our device. Figs. 7(a) and (b) show the RC-limited, measured O-E, fitted O-E, and transient time limited frequency responses of devices A and B, respectively. The bias voltages for device A and B is the same at −13 V. Note that the RC-limited bandwidth exhibited by device B is close to the transient-time-limited value of around 30 GHz. This indicates that the total depletion layer thickness is nearly optimized to balance the internal carrier transit time and external RC-limited time constant for the case of a 25 μm active diameter. On the other hand, device A has an RC-limited O-E bandwidth, and a wider 3-dB O-E bandwidth can be expected by further downscaling its active diameter.

Figs. 8(a) and (b) show the dc output photocurrent versus input optical power of devices A and B, respectively. The 1-dB compression current of each device is specified on this Figure. As can be seen, under a nearly V_{br} bias, the dc saturation current of device A is higher than that of device B (5 vs. 3 mA) due

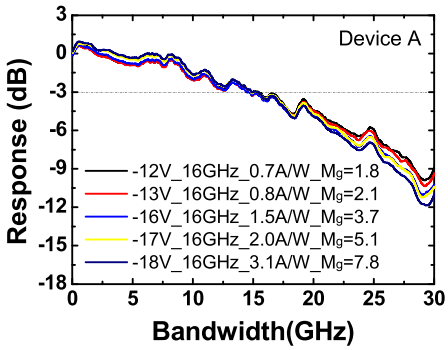

Fig. 9. The measured bias dependent O-E frequency responses of device A under an optical pumping power of 1 mW at the 1.31 μm wavelength.

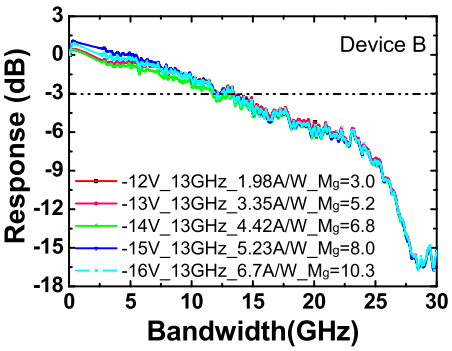

Fig. 10. The measured bias dependent O-E frequency responses of device B under an optical pumping power of 0.5 mW at the 1.31 μm wavelength.

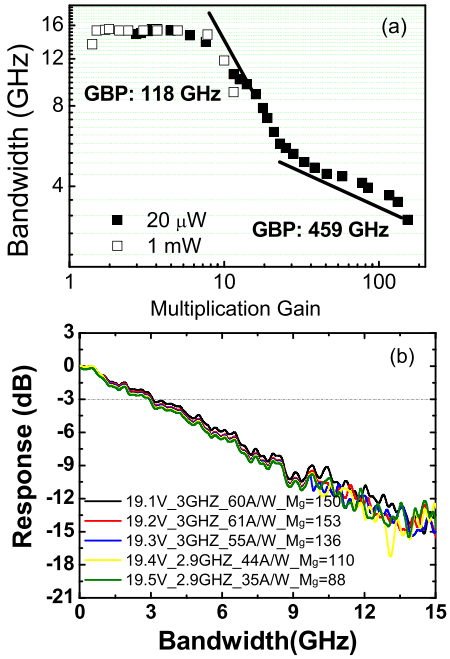

Fig. 11. (a) The measured 3-dB O-E bandwidths versus multiplication gain of device A at low (20 μW) and high (1 mW) optical pumping powers. (b) The measured O-E frequency responses of device A under low power (20 μW) and high gain operation.

to the thinner depletion layer thickness, as discussed above. By assuming an output photocurrent of 1 mA with a uniform distribution across the 12 μm diameter of the active window in both devices and a constant hole drift-velocity of 5.3×10^4 m/sec [18] across the depletion layer, the calculated SCS E-field induced by the photo-generated holes is as small as around 5.1 and 7.9 kV/cm for devices A and B, respectively [25]. Such values are much smaller than the static E-field in the absorber (>100 kV/cm) and multiplication layer (>900 kV/cm) under near V_{br} operation. The influence of the SCS effect on the drift-velocity of the carriers in our device under high-power operation should thus be negligible. Nevertheless, based on McIntyre's model [26], the avalanche gain is very sensitive to the E-field in the M-layer, especially under high-gain operation. Even such a small change in the E-field will result in a pronounced variation in the multiplication gain. This explains why we can still see such a significant difference in the saturation current and operation gain between devices A and B under high-power operation.

It is reported the for most high-speed p-i-n PDs, a saturation in their dc output current is accompanied by serious degradation in the O-E bandwidth and saturation in the photo-generated RF power. Figs. 9 and 10 show the bias dependent O-E frequency responses of devices A and B measured under saturated input optical power (1 and 0.5 mW, respectively). As can be seen, the 3-dB O-E bandwidths for devices A and B are pinned at 16 and 13 GHz, respectively, under different reverse bias voltages. These bandwidth values are close to the maximum O-E bandwidths of both devices measured under low power excitation, as shown in Figs. 4 and 5. The superior high-power performance of our APDs compared to traditional p-i-n PDs can be attributed to that the speed performance of the APD being limited by the avalanche induced delay time rather than the transit time across the depleted absorption region in the p-i-n PD. As can be seen in Figs. 2 and 3, there is a significant reduction in the operation gains of both devices with an increase in the optical pumping power. In addition, the values of the operation gain become much less sensitive to the reverse bias voltage under high-power operation. These results explain the enhancement in speed performance and the invariant 3-dB O-E bandwidth of both devices under different bias voltages and high-power operation. Although the gain reduction happens under high-power operation, the achieved saturation current (>5 mA) and responsivity (3.1 A/W) of device A under nearly V_{br} operation are superior to those of typical p-i-n photodiodes, with a close value of bandwidth [18].

Fig. 11(a) shows the 3-dB O-E bandwidths versus operation gains of device A measured under low (20 μW) and high (1 mW) optical pumping powers. As can be seen, for the low pumping power case, our demonstrated device can achieve a gain-bandwidth (GB) product as high as 459 GHz with a 38% unit-gain external efficiency. On the other hand, there is a gradual decrease in the values of the GB product gradually to 118 GHz when the optical pumping power reaches 1 mW, which can be attributed to the reduction in the multiplication gain versus the increase of optical power, as discussed above. The achieved high GB product (459 GHz) can be attributed to the aggressive

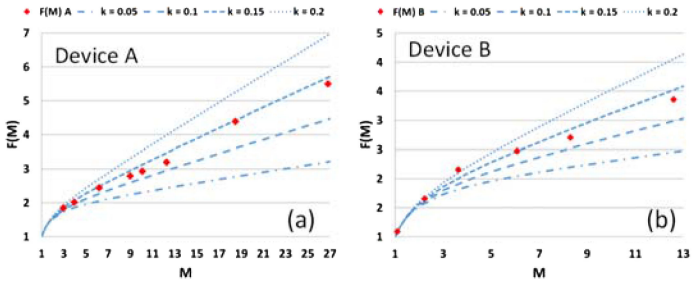

Fig. 12. Excess noise factor against gain of (a) devices A and (b) B.

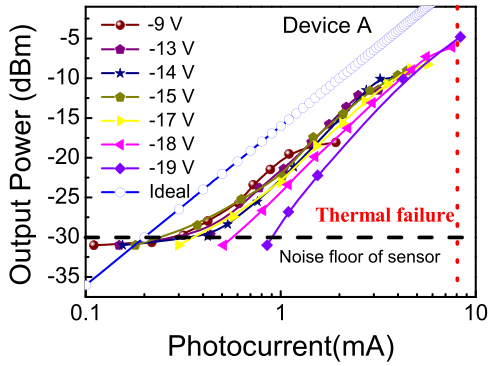

Fig. 13. The measured photo-generated microwave power versus photocurrent of device A under different reverse biases at operating frequencies of 15 GHz. The open symbol line shows the ideal trace for a 100% optical modulation depth and 50 Ω load.

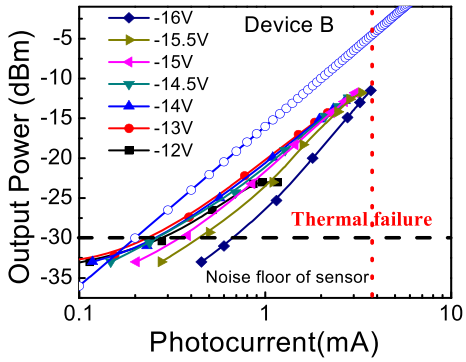

Fig. 14. The measured photo-generated microwave power versus photocurrent of device B under different reverse biases at an operating frequency of 15 GHz. The line of open symbols shows the ideal trace for a 100% optical modulation depth and 50 Ω load.

downscaling of the M-layer and the absorber thicknesses and the significant dead space effect inside the M-layer [27]. Furthermore, compared to the gain-bandwidth curves of typical APDs, which usually exhibit monotonic decreases of bandwidth with the increase of the multiplication gain [22], our devices exhibit different trends in these curves. As can be seen, under very-high operation gain (>30), the decrease in bandwidth vs. the gain is gradually minimized. Fig. 11(b) shows the corresponding O-E responses measured under high-gain and low power (20 μW) operation. We can clearly see that the measured bandwidth is pinned at around 3 GHz no matter how much larger the gain is, thereby resulting in the high gain-bandwidth product (459 GHz) we obtain. A possible mechanism for this phenomena can be understood as follows. As shown in Fig. 1, the major difference between our device's structure and that of the typical fast APDs is that there are an extra charge and thin (60 nm) $In_{0.52}Al_{0.48}As$ field buffer layers above the 88 nm M-layer. Under lower bias (gain), such a thin (60 nm) buffer layer is not able to contribute to significant gain and the gain-bandwidth curve thus behaves like a normal high-speed APD. On the other hand, under a near V_{br} bias, such thin layers begin to allow significant multiplication gain. This can avoid the 88 nm M-layer being pushed into the deep avalanche region for very high-gain operation, thereby releasing the bandwidth reduction under near V_{br} operation. Using the Monte Carlo method to simulate in detail and explain the distinct dynamic behaviors of this device will be the direction of our future research [28].

Furthermore, the high GB product in an APD with a thin multiplication layer is usually accompanied by little excess noise and a small k-factor [27]. The noise floor in the APD is usually determined by its shot noise, which is proportional to the total current (dark current plus photocurrent) multiplied by the excess noise factor (F) and the square of the multiplication gain (M) [29] (FM^2). A smaller k-factor can greatly reduce the (FM^2) product thereby lowering the noise floor in APD based receivers for wide dynamic range performance. Fig. 12 shows the measured excess noise (F(M)) versus multiplication gain (M) of these two devices at 1310 nm wavelength. For details about the excess noise measurement setup please refer to our previous work [30]. The extracted k-factors for devices A and B are very close at around 0.14 due to their same M-layer thickness as 88 nm. Comparison to the k-factor values (∼0.15) reported for $In_{0.52}Al_{0.48}As$ APDs with the same M-layer thickness (90 nm) as ours [15] shows our device to have comparable or smaller k-factors due to its larger GB product, as discussed above.

The output saturation power of our demonstrated APD is tested using a two-laser heterodyne-beating setup at the 1550 nm wavelength. Figs. 13 and 14 show the measured photo-generated RF power versus output photocurrent obtained under different reverse biases. The measurement frequency was selected to be around the 3-dB O-E bandwidth for both devices A and B at 15 GHz. The ideal relation between the microwave power and averaged photocurrent (solid line), with a 100% optical modulation depth under a 50 Ω load, is also plotted for reference. We can clearly see that the photo-generated RF power of both devices A and B shows no significant saturation even when the output photocurrent is above their dc saturation currents of 5 and 3 mA, respectively. This behavior is in contrast to the typical high-speed p-i-n PDs, which always show saturation in the photo-generated RF power when their output averaged dc current is near saturation. In addition, under a small output photocurrent (< 1mA), the nearly V_{br} bias of both devices would lead to a photo-generated RF power far below the ideal power values on a 50 Ω load. On the other hand, when the output photocurrent increases, all the traces measured under different

reverse bias voltages merge together, which can be attributed to the reduction in the avalanche delay time and enhancement of the O-E bandwidth under high-power operation, as discussed in Figs. 9 and 10. As can be seen, the highest output photocurrents for maximum output RF power for devices A and B occur at 8 and 4 mA, respectively, and are limited by thermal failure, due to the required high bias voltages. Overall, the high-speed (16 GHz), high-responsivity (2.5 A/W at 0.9 V_{br}), high output photocurrent (8 mA), and low excess noise of the demonstrated APDs demonstrate their strong potential for replacing fast p-i-n PDs in coherent receivers. The photocurrent of the homodyne beating signal in the receiving end is linearly proportional to the responsivity of the photodetector [31]. The higher responsivity (2.5 vs. 0.9 A/W) of device A can thus provide around 8 dB higher RF beating power than those of commercially available 10 Gbit/sec p-i-n PDs under the same optical LO pumping power of 1 mW. Although the saturation optical power of the p-i-n PD is usually higher than 1 mW, significant enhancement of the S/N ratio by further increasing the optical LO power in the p-i-n based PD receiving end may not be feasible due to the very limited optical LO power in the chip scale or PIC FMCW lidars, as discussed in [5], [10], [11]. In short, the main advantage of our proposed wide dynamic range APD is enhancement of the S/N ratio in the coherent receiver with much less required optical LO power.

Compared to the reported high-performance waveguide type balanced APDs designed for homodyne coherent fiber communication [32], our demonstrated device A has a smaller 3-dB O-E bandwidth (16 vs. 20 GHz at 0.9 V_{br}) but a higher bandwidth-responsivity product (183.6 vs. 147 GHz $\times$ A/W) and a much higher RF power output (-5 vs. -15 dBm) under the same optical pumping power (0 dBm). In addition, compared with the reported dual-carrier injection APD designed for high-linearity performance with a backside-illuminated structure [15], [33], [34], our top-illuminated structures (for both A and B) can deliver a comparable 1 dB compression (90%) current ($\sim$1.4 mA), as specified in Fig. 8, under M $=$ 10 operation. The measured responsivity of device B is comparable to that of such an APD ($\sim$7 A/W) under M $=$ 10 operation [15], [33], [34].

IV. Conclusion

In conclusion, we demonstrate novel top-illuminated APD structures with excellent performance for coherent lidar applications. By downscaling the partially p-doped $In_{0.53}Ga_{0.47}As$ absorber to minimize the SCS effect in the multiplication layers, we produce a device with faster speed performance and higher saturation currents than those of references with a thicker absorber (0.8 vs. 0.4 μm). Our demonstrated APD can achieve a wide O-E bandwidth (16 GHz), high responsivity (2.5 A/W at 0.9 V_{br}), and low excess noise (k $=$ 0.14) under a near saturation output current ($\sim$8 mA at 1 mW pumping power). Furthermore, such a device can eliminate degradation in the O-E bandwidth and sustain high-speed performance at the saturation output photocurrent due to the reduction in the operation gain and shortening of the avalanche delay time with an increase in the optical pumping power. Such excellent dynamic performance is in contrast to that of the high-speed p-i-n PD, which typically shows serious degradation in the O-E bandwidth near the saturation output photocurrent. The APDs demonstrated excellent dynamic/static performance, opening up new ways to further improve the performance of coherent lidar receivers.

References

[1] J.-W. Shi, J.-In Guo, M. Kagami, P. Suni, and O. Ziemann, "Photonic technologies for autonomous cars: Feature introduction," *Opt. Exp.*, vol. 27, pp. 7627–7628, Mar. 2019, doi: 10.1364/OE.27.007627.

[2] [Online]. Available: http://www.woodsidecap.com/wp-content/uploads/2018/04/Yole_WCP-LiDAR-Report_April-2018-FINAL.pdf

[3] J. Hecht, "Lidar for self-driving cars," *Opt. Photon. News*, vol. 29, no 1, pp. 26–33, Jan. 2018.

[4] C. V. Poulton, A. Yaacobi, D. B. Cole, M. J. Byrd, M. Raval, D. Vermeulen, and M. R. Watts, "Coherent solid-state lidar with silicon photonic optical phased arrays," *Opt. Lett.*, vol. 42, no. 20, pp. 4091–4094, Oct. 2017, doi: 10.1364/OL.42.004091.

[5] P. J. M. Suni, J. E. Bowers, Larry Coldren, and S. J. Ben Yoo, "Photonic integrated circuits for coherent lidar," in *Proc 18th Coherent Laser Radar Conf.*, Boulder, CO, USA, Jun. 2016, pp. 1–6

[6] S. Crouch, "Advantages of 3D imaging coherent lidar for autonomous driving applications," in *Proc. 19th Coherent Laser Radar Conf.*, Okinawa, Japan, Jun. 2018, pp. 1–4.

[7] B. F. Aull, E. K. Duerr, J. P. Frechette, K. A. McIntosh, D. R. Schuette, and R. D. Younger, "Large-format geiger-mode avalanche photodiode arrays and readout circuits," *IEEE J. Sel. Topics Quantum Electron.*, vol. 24, no. 2, pp. 1–10, Mar./Apr. 2018, Art. no. 3800510, doi: 10.1109/JSTQE.2017.2736440.

[8] J. W. Raring *et al.*, "40 Gbit/s photonic receivers integrating UTC photodiodes with high- and low-confinement SOAs using quantum well intermixing and MOCVD regrowth," *Electron. Lett.*, vol. 42, no. 16, pp. 942–943, Aug. 2006, doi: 10.1049/el:20061368.

[9] M. Anagnosti *et al.*, "Record gain x bandwidth (6.1 THz) monolithically integrated SOA-UTC photoreceiver for 100-Gbit/s applications," *J. Lightw. Technol.*, vol. 33, no. 6, pp. 1186–1190, Mar. 2015, doi: 10.1109/JLT.2014.2372816.

[10] B. Behroozpour, P. A. M. Sandborn, N. Quack, T. J. Seok, Y. Matsui, Ming C. Wu, and B. E. Boser, "Chip-scale electro-optical 3D FMCW lidar with 8μm ranging precision," in *Proc. Int. Solid-State Circuits Conf. Dig. Tech. Papers*, San Francisco, CA, USA, Feb. 2016, pp. 214–215.

[11] A. Martin *et al.*, "Photonic integrated circuit-based FMCW coherent lidar," *J. Lightw. Technol.*, vol. 36, no. 19, pp. 4640–4645, Oct. 2018, doi: 10.1109/JLT.2018.2840223.

[12] J.-M. Wun, C.-C. Wei, J. Chen, C. S. Goh, S. Y. Set, and J.-W. Shi, "Photonic chirped radio-frequency generator with ultra-fast sweeping rate and ultra-wide sweeping range," *Opt. Exp.*, vol. 21, no. 9, pp. 11475–11481, May 2013, doi: 10.1364/OE.21.011475.

[13] T. Hariyama, P. A. M. Sandborn, M. Watanabe, and M. C. Wu, "High-accuracy range-sensing system based on FMCW using low-cost VCSEL," *Opt. Exp.*, vol. 26, no. 7, pp. 9285–9297, Apr. 2018, doi: 10.1364/OE.26.009285.

[14] H.-Y. Zhao, Naseem, A. H. Jones, J. C. Campbell, and J.-W. Shi, "High-speed and wide dynamic range avalanche photodiode for coherent lidar application," in *Proc. IEEE Photon. Soc. Meeting*, San Antonio, TX, USA, Sep. 2019, pp. TuE1.1.

[15] M. Nada, Y. Yamada, and H. Matsuzaki, "Responsivity-bandwidth limit of avalanche photodiodes: Toward further Ethernet systems," *IEEE J. Sel. Topics Quantum Electron.*, vol. 24, no. 2, pp. 1–11, Mar./Apr. 2018, Art. no. 3800811, doi: 10.1109/JSTQE.2017.2754361.

[16] Y.-H. Chen *et al.*, "Top-illuminated $In_{0.52}Al_{0.48}As$-based avalanche photodiode with dual charge layers for high-speed and low dark current performances," *IEEE J. Sel. Top. Quantum Electron.*, vol. 24, no. 2, pp. 1–8, Mar.–Apr. 2018, Art. no. 3800208, doi: 10.1109/JSTQE.2017.2731938.

[17] S.-L. Wu *et al.*, "High-Speed In0.52Al0.48 As Based Avalanche Photodiode with Top-Illuminated Design for 100 Gbit/sec ER-4 System," *IEEE/OSA J. Lightwave Tech.*, vol. 36, pp. 5505–5510, Dec. 2018.

[18] K. Kato, "Ultrawide-band/high-frequency photodetectors," *IEEE Trans. Microw. Theory Techn.*, vol. 47, no. 7, pp. 1265–1281, Jul. 1999, doi: 10.1109/22.775466.

[19] J.-W. Shi *et al.*, "Separated-transport-recombination p-i-n photodiode for high-speed and high-power performance" *IEEE Photon. Technol. Lett.*, vol. 17, no. 8, pp. 1722–1724, Aug. 2005, doi: 10.1109/LPT.2005.850886.
[20] M. S. Park and J. H. Jang, "$GaAs_{0.5}Sb_{0.5}$ lattice matched to InP for 1.55 μm photo-detection," *Electron. Lett.*, vol. 44, no. 8, pp. 549–551, Apr. 2008, doi: 10.1049/el:20083433.
[21] M. Nada, Y. Muramoto, H. Yokoyama, and H. Matsuzaki, "High-speed high-power-tolerant avalanche photodiode for 100-Gb/s applications," in *Proc. IEEE Photon. Soc. Meeting*, San Diego, CA, USA, 2014, Paper TuA1.4.
[22] J. C. Campbell *et al.*, "Recent advances in avalanche photodiodes," *IEEE J. Sel. Top. Quantum Electron.*, vol. 10, no. 4, pp. 777–787, Jul.–Aug. 2004, doi: 10.1109/JSTQE.2004.833971.
[23] Y.-S. Wu, J.-W. Shi, and P.-H. Chiu, "Analytical modeling of a high-performance near-ballistic uni-traveling-carrier photodiode at a 1.55μm wavelength," *IEEE Photon. Technol. Lett.*, vol. 18, no. 8, pp. 938–940, Apr. 2006, doi: 10.1109/LPT.2006.873567.
[24] Z. A.. Naseem *et al.*, "The enhancement in speed and responsivity of uni-traveling carrier photodiodes with $GaAs_{0.5}Sb_{0.5}$/$In_{0.53}Ga_{0.47}As$ type-II hybrid absorbers," *Opt. Exp.*, vol. 27, no. 11, pp. 15495–15504, May 2019, doi: 10.1364/OE.27.015495.
[25] J.-W. Shi, F.-M. Kuo, and J. E. Bowers, "Design and analysis of ultra-high speed near-ballistic uni-traveling-carrier photodiodes under a 50 Ω load for high-power performance," *IEEE Photon. Technol. Lett.*, vol. 24, no. 7, pp. 533–535, Apr. 2012, doi: 10.1109/LPT.2011.2179795.
[26] R. J. McIntyre, "Multiplication noise in uniform avalanche diodes," *IEEE Trans. Electron Devices*, vol. ED-3, no. 1, pp. 164–168, Jan. 1966, doi: 10.1109/T-ED.1966.15651.
[27] M. A. Saleh *et al.*, "Impact-ionization and noise characteristics of thin III-V avalanche photodiodes," *IEEE Trans. Electron Devices*, vol. 48, no. 12, pp. 2722–2731, Dec. 2001, doi: 10.1109/16.974696.
[28] W. Sun, X. Zheng, Z. Lu, and J. C. Campbell, "Monte Carlo simulation of InAlAs/InAlGaAs tandem avalanche photodiodes," *IEEE J. Quantum Electron.*, vol. 48, no. 4, pp. 528–532, Apr. 2012, doi: 10.1109/JQE.2012.2187046.
[29] M. Huang *et al.*, "Germanium on silicon avalanche photodiode," *IEEE J. Sel. Top. Quantum Electron.*, vol. 24, no. 2, pp. 1–11, Mar.–Apr. 2018, Art. no. 3800911, doi: 10.1109/JSTQE.2017.2749958.
[30] H.-D. Liu *et al.*, "Avalanche photodiode punch-through gain determination through excess noise analysis," *J. Appl. Phys.*, vol. 106, Sep. 2009, Art. no. 064507, doi: 10.1063/1.3226659.
[31] P. Adany, C. Allen, and R. Hui, "Chirped lidar using simplified homodyne detection," *J. Lightw. Technol.*, vol. 27, no. 16, pp. 3351–3357, Aug. 2009, doi: 10.1109/JLT.2009.2016220.
[32] P. Runge *et al.*, "Waveguide integrated balanced photodetectors for coherent receivers," *IEEE J. Sel. Top. Quantum Electron.*, vol. 24, no. 2, pp. 1–7, Mar.–Apr. 2018, doi: 10.1109/JSTQE.2017.2723844.
[33] M. Nada, Y. Yamada, and H. Matsuzaki, "A high-linearity avalanche photodiodes with a dual-carrier injection structure," *IEEE Photon. Technol. Lett*, vol. 29, no. 21, pp. 1828–1831, Nov. 2017, doi: 10.1109/LPT.2017.2753262.
[34] M. Nada, F. Nakajima, T. Yoshimatsu, H. Matsuzaki, and K. Sano, "High-speed avalanche photodiodes based on III-V compounds for optical communications," in *Proc. Compound Semicond. Week*, Nara, Japan, May 2019, Paper ThB2–1.

Hao-Yi Zhao was born in Taichung, Taiwan on February 21, 1995. He received the B.S. degree from the Department of Electrical Engineering, Feng Chia University, Taichung, Taiwan. He is currently working toward the master's degree at the Department of Electrical Engineering, Feng Chia University, National Central University, Taoyuan, Taiwan.

His current research interests include high-speed PDs.

Naseem was born in Punjab, India, in 1991. He received the M. Tech. degree from the Department of Nanotechnology, Jamia Millia Islamia, New Delhi, India. He is currently working toward the Ph.D. degree at the Department of Electrical Engineering, National Central University, Taoyuan, Taiwan. His current research interests include high-speed photodiodes and avalanche photodiodes for optical receivers.

Andrew H. Jones received the B.S. degree in electrical engineering from Grove City College, Grove City, PA, USA, in 2014. He is currently working toward the Ph.D. degree in electrical engineering at the University of Virginia, Charlottesville, VA, USA. His research interests lie in III–V photonic devices, specifically for infrared applications.

Rui-Lin Chao was born in Taipei, Taiwan on October, 27, 1991. He received the B.S. degree from the Undergraduate Honors Program of Nano Science and Engineering, Chiao Tung University, Hsinchu, Taiwan, in 2014, and now is working toward the Ph.D. degree in the Department of Elecro-Optics, Chiao Tung University, under the guidance of Prof. Jyehong Chen, and co-advisor Prof. Jin-Wei Shi, National Central University, focusing on slow light high speed silicon based modulator, high speed photodetector, and high speed laser development and design.

Zohauddin Ahmad was born in Bihar, India, in 1989. He graduated from Department of Nanoscience and Nanotechnology, Jamia Millia Islamia, New Delhi, India. He is currently working toward the Ph.D. degree at Department of Electrical Engineering, National Central University, Taoyuan, Taiwan. His current research includes high-speed modulator-based lasers, high-speed VCSELs, and photonics integrated circuits.

Joe C. Campbell (M'74–F'90) received the B.S. degree in physics from the University of Texas at Austin, Austin, TX, USA, in 1969, and the M.S. and Ph.D. degrees in physics from the University of Illinois at Urbana-Champaign, Urbana, IL, USA, in 1971 and 1973, respectively. From 1974 to 1976, he was employed by Texas Instruments where he worked on integrated optics. In 1976, he joined the staff of AT&T Bell Laboratories in Holmdel, NJ, USA. In the Crawford Hill Laboratory, he worked on a variety of optoelectronic devices including semiconductor lasers, optical modulators, waveguide switches, photonic integrated circuits, and photodetectors with emphasis on high-speed avalanche photodiodes for high-bit-rate lightwave systems. In January of 1989, he joined the faculty of the University of Texas at Austin as Professor of Electrical and Computer Engineering and Cockrell Family Regents Chair in Engineering. In January of 2006, he became a member of the faculty at the University of Virginia in Charlottesville as the Lucian Carr, III Chair of Electrical Engineering and Applied Science. His research has focused on the optoelectronic components that are used to generate, modulate, and detect the optical signals. At present, he is actively involved in single-photon-counting avalanche photodiodes, Si-based optoelectronics, high-speed, low-noise avalanche photodiodes, ultraviolet photodetectors, and quantum-dot IR imaging. To date, he has coauthored 10 book chapters, 450 articles for refereed technical journals, and more than 400 conference presentations.

Prof. Campbell is a member of the National Academy of Engineering.

Jin-Wei Shi (M'03–SM'12) was born in Kaohsiung, Taiwan on January 22, 1976. In 2003, he joined the Department of Electrical Engineering, National Central University, Taoyuan, Taiwan, where he has served as a Professor from 2011. In 2011–2012 and 2016–2017, he joined the Department of Electrical and Computer Engineering (ECE), University of California, Santa Barbara (UCSB) as a Visiting Professor. His current research interests include ultra-high speed/power photodetectors, electro-absorption modulator, THz photonic transmitter, and VCSELs. He has authored or coauthored more than 4 book chapters, 150 journal papers, 200 conference papers, and holds 30 patents.

Prof. Shi was the recipient of the 2010 Da-You Wu Memorial Award.